Anomaly Detection Method With Rebar Response Suppression for Microwave Ground Penetrating Radar Pavement Inspection

Natsuki Akiyama, Takahide Morooka, Katsuyoshi Suzuki ⓘ, and Shouhei Kidera ⓘ, *Senior Member, IEEE*

Abstract—Unsupervised anomaly detection analysis using rebar response rejection is presented for microwave ground penetrating radar (GPR)-based pavement inspections. Various approaches have been used to detect cracks, water, or corrosion in buried objects in the GPR model using synthetic aperture radar (SAR) image. However, this does not always accurately identify an anomaly state because the SAR image largely depends on the selected propagation model (e.g., relative permittivity of background concrete media) or suffers from unnecessary responses such as those from rebars. To address this issue, this article first introduces an effective clutter rejection scheme focusing on the rebar response, using transfer-function-based signal extraction to identify anomalous responses from the boundary between the asphalt and its floorboard. Moreover, we introduce several unsupervised anomaly detection algorithms for time–frequency response data if a large part of the investigation area has normal reflection responses. We performed experimental tests on data from real roads in need of repair to validate that our approach can detect internal anomalies in asphalt or its floorboard.

Index Terms—Anomaly detection, clutter rejection signal processing, ground penetrating radar (GPR), microwave pavement inspections, time–frequency (TF) analysis, unsupervised machine learning.

I. INTRODUCTION

DETECTION of air cracks or metallic rust in aging bridges, tunnels, and highway roads is an emerging requirement that has rapidly increased in recent years in Japan and other developed countries. Microwave ground penetrating radar (GPR) techniques have been gaining attention to meet the high demand for the rapid, large-scale monitoring of the transportation infrastructure, e.g., pavement investigations [1], [2], [3], [4], because they perform noncontact measurement with deep penetration depths in concrete media, which is advantageous over sound or ultrasonic diagnosis. Pioneering research on microwave investigation was first conducted with a focus on ceramics [5]. Several

studies since then have demonstrated that significant differences in dielectric properties among various types of rust, e.g., black, salt, and red rust [6], [7]. This variation has accelerated the development of microwave testing approaches, for instance, with the use of waveguide probes (e.g., in metal corrosion monitoring) [8], [9]. In addition, microwave radar imaging approaches, e.g., synthetic aperture radar (SAR) [10], [11] polarimetric SAR [12], and other migration algorithms [13], [14] can extract the spatial profiles of the reflection coefficients of target objects with low complexity. In recent years, tomography-based approaches such as permittivity estimation for multilayered media [15], full wave inversion [16], and contrast source inversion (CSI) [17] have been implemented, where domain integral equations derived from the Helmholtz equation are numerically solved using various optimizers.

However, each radar and tomographic approach has specific problems. Radar imaging cannot quantitatively estimate the complex permittivity of buried objects, which can significantly vary in different material types, including air, water, saline, and corroded steel. In addition, the reconstruction accuracy of radar images largely depends on the assumed relative permittivity of the background media, such as asphalt and floorboards with concrete materials, whose permittivity varies significantly under wet conditions. Conversely, tomography, i.e., inverse scattering analysis, can provide the quantitative dielectric profiles of objects. However, this inverse problem is nonlinear and usually incurs high computational costs in cases involving 3-D models of large-scale investigation areas. Various tomography approaches have been proposed to solve the problem in the nonlinearity, e.g., as Born approximation-based methods [18], [19], [20], [21], [22], CSI [23], [24], [25], [26], [27], [28], or other inversion approaches [29], [30]. The CSI markedly reduces computational costs by avoiding the iterative use of a forward solver, although the number of unknowns is much larger than that of measurements (ill-posed condition), which is disadvantageous in large-volume 3-D analysis. While several studies have explored the integration of radar and inverse scattering techniques, managing large-scale areas over 100 wavelengths (approximately 10 m) remains a significant challenge due to the impractical computational demands of the inversion process [31], [32].

Herein, we present an anomaly detection approach that uses different outlier detection methods, where raw data or time–frequency (TF) responses are input into an unsupervised learning scheme. Although many papers have studied optical

image-based anomaly detection for pavement surface inspections [33], [34], [35], [36], [37], [38], [39], these methods are designed to detect a surface crack, and cannot detect internal anomalies. Sound or ultrasound-based machine learning approaches have also been developed for identifying cracks or other abnormal objects buried in concrete media [40], [41], [42], [43], [44], although these approaches required contact measurement, which hinders a speedy survey. Conversely, microwave GPR offers deeper noncontact measurement, and several studies have focused on B-scan data-based anomaly detection. It is an acceptable presumption in an actual pavement investigations that a large portion of the investigation area, e.g., a road or tunnel wall, is assumed to be in a healthy state and will provide similar responses. Thus, an area where raw data significantly deviate from the average response is predicted to be in an abnormal state, possibly due to cracks, water leakage, or corrosion. Significantly, numerous studies have focused on anomaly detection in GPR data using supervised machine learning approaches [45], [46]. These methods require extensive datasets for training, which include data on normal and anomalous conditions, and account for various road structure models and anomaly characteristics such as thickness, shape, or dielectric parameters. In contrast, our proposed method employs an unsupervised outlier detection approach, which eliminates the need for a training dataset and is widely applicable to a diverse range of road models based on the aforementioned assumptions.

In addition, this study first introduces an efficient suppression scheme for rebar responses to extract anomaly responses caused by cracks or water leakage, which predominantly occur in the boundary area between the asphalt and the floorboard. This rebar suppression scheme adopts a reference signal-based transfer function (TRF) approach, that retains target signals deeper than the rebar position. While a number of rebar response suppression schemes have been introduced, such as F-K filtering [47], [48], [49], these approaches may also suppress responses from anomaly areas that have similar frequency and wavenumber responses. Focusing on anomaly detection using B-scan data, this article introduces four unsupervised outlier detection algorithms, namely, the Mahalanobis distance (MD), cross-correlation index (CCI) with frequency-range profiles, convolutional autoencoder (CAE), and density-based spatial clustering of applications with noise (DBSCAN). These algorithms are then applied to measurement data from different areas on real pavements frequently investigated by the Japanese Ministry of Infrastructure to avoid severe accidents due to earthquakes or aging effects. Different anomaly detection analyses demonstrate that our proposed schemes can provide significant information for the identification of anomalous areas in a cost-effective manner for large-scale surveys.

The main contributions of this study are summarized as follows.

1) An anomaly detection scheme for microwave GPR data is proposed without using a computationally demanding imaging analysis.
2) A novel rebar-response-suppression scheme that uses the TRF process to specifically extract hyperbolic rebar responses from B-scan data, which is rarely achieved by the
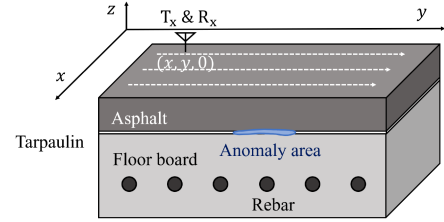

Fig. 1. GPR observation model with asphalt and floorboard layers-based media, including anomaly area.

traditional windowing-based suppression scheme. Importantly, this rebar suppression can detect anomaly features between asphalt and floorboards.
3) A computationally effective and unsupervised anomaly detection scheme is presented by exploiting B-scan data, (e.g., TF response by combining the proposed rebar suppression scheme). An application of existing anomaly-detection algorithms provides integrated indexes that offer the most reliable results for anomaly area detection.
4) Experimental data from real road scenario demonstrates the effectiveness of the proposed scheme for both rebar response suppression and anomaly state detection, especially for the Shin-tone bride pavement with free-lime area (referential anomaly state area).

II. METHOD

A. Observation Model

Fig. 1 shows the observation model assumed in typical pavement inspection cases. A transmitter and a receiver with a fixed offset are scanned on the $z = 0$ plane. The center of the transmitter and receiver is defined as $(x, y, 0)$, and the recorded signal at each location is denoted as $s'(x, y, t)$, where t is time. The signal is converted into $s'(x, y, R)$ using the relationship $R = c_{air}t/2$ with the propagation speed in air c_{air}. A matched filter response is applied to $s'(x, y, R)$, where the reference signal is defined as the transmitted signal. The reflection from a concrete surface is eliminated from averaged responses to remove the interfering effects caused by inconsistency, e.g., surface crack. The resulting processed signal is defined as $s(x, y, R)$.

B. Preprocessing of B-SCAN GPR Data

To focus on anomaly detection in an internal area of asphalt (upper media) and the boundary area of the upper surface of a concrete floorboard, the rebar responses, which are usually observed in deep areas, should be suppressed before detection. The following window function-based approach is a simple suppression method, where deep responses at a specific depth are eliminated by the traditional raised cosine based roll-off window function [50] $W(R; R_{FL}, \alpha)$ as: (1) shown at the bottom of the next page.

The suppression signal is then calculated as

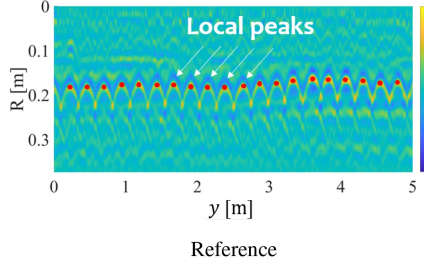$$s_{sup}^{W}(x, y, R) = W(R; R_{FL}, \alpha)s(x, y, R) \qquad (2)$$

Fig. 2. Referential response for rebar suppression scheme as $s_{\text{ref}}(x_i, y, R)$ and the extracted local peaks of rebar hyperbolic responses (red dots) as (y_j, R_j).

Fig. 3. Extracted rebar responses as $\bar{h}_{\text{rebar}}(y, R)$ and the reber responses area as Ω_{rebar} used in (5) in the proposed scheme.

where the α denotes the roll-off factor, and R_{FL} denotes the filter length (FL) along R. However, the window-based approaches pose several risks for over- or insufficient suppression because the depths of rebar responses are not always constant and the erroneous setting of R_{FL} can unnecessarily suppress floorboard responses or undersuppress rebar responses.

1) TRF-Based Rebar Response Extraction: To overcome the aforementioned difficulty, this study originally introduces a rebar response suppression scheme using TRF-based deconvolution. Let $s_{\text{ref}}(x_i, y, R)$ be the reference response, which includes the number of rebars and denotes the extracted scan line as $x = x_i$. Then, the function $d_{\text{ref}}(x_i, y, R)$ is calculated as

$$d_{\text{ref}}(x_i, y, R) = \sum_{j=1}^{N_{\text{p}}} |s_{\text{ref}}(x_i, y_j, R_j)| \delta(y - y_j, R - R_j)$$
(3)

where (y_j, R_j) is extracted from the local maximum of the jth hyperbolic rebar responses of $s_{\text{ref}}(x_i, y, R)$, and N_{p} indicates the number of those local maxima. $\delta(y, R)$ is the 2-D Dirac delta function in the (y, R) space, as shown in Fig. 2. Then, the TRF of the rebar response, denoted as $H_{\text{rebar}}(x_i, k_y, k_R)$, is calculated as

$$H_{\text{rebar}}(x_i, k_y, k_R) = \frac{S_{\text{ref}}(x_i, k_y, k_R)}{D_{\text{ref}}(x_i, k_y, k_R)}$$
(4)

where $S_{\text{ref}}(x_i, k_y, k_R)$ and $D_{\text{ref}}(x_i, k_y, k_R)$ denote the 2-D Fourier transforms of $s_{\text{ref}}(x_i, y, R)$ and $d_{\text{ref}}(x_i, y, R)$, respectively, for y and R. $h_{\text{rebar}}(x_i, y, R)$ is the 2-D inverse Fourier transform of $H_{\text{rebar}}(x_i, k_y, k_R)$. The average rebar response is calculated as

$$\bar{h}_{\text{rebar}}(y, R) = \begin{cases} \frac{1}{N_{\text{x}}} \sum_{i=1}^{N_{\text{x}}} h_{\text{rebar}}(x_i, y, R), & ((y, R) \in \Omega_{\text{rebar}}) \\ 0, & ((y, R) \notin \Omega_{\text{rebar}}) \end{cases}$$
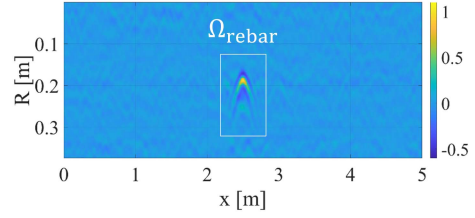(5)

where N_{x} denotes the number of scans of the reference data along x samples, and Ω_{rebar} is the area covering the rebar hyperbolic responses, as shown in Fig. 3.

2) Rebar Response Suppression: The rebar responses are suppressed using $\bar{h}_{\text{rebar}}(y, R)$. Automatic extraction of the peak position as $(\hat{y}_j, \hat{R}_j; x_i)$ is presented to accelerate the preprocessing scheme. Assuming the measurement signal $s(x_i, y, R)$, we apply deconvolution as

$$\tilde{D}(x, k_y, k_R) = \frac{S(x, k_y, k_R)}{H_{\text{rebar}}(x, k_y, k_R)}.$$
(6)

Then, the peak positions $(\hat{y}_j, \hat{R}_j; x_i)$ are extracted from

$$\left. \begin{array}{r} \partial |\tilde{d}(x, y, R)| / \partial y = 0 \\ \partial |\tilde{d}(x, y, R)| / \partial R = 0 \\ |\tilde{d}(x, y, R)| \geq \beta \max_{y, R} |\tilde{d}(x, y, R)| \end{array} \right\}$$
(7)

where $\tilde{d}(x, y, R)$ is the 2-D inverse Fourier transform of $\tilde{D}(x, k_y, k_R)$. β is a constant threshold. Then, similar to (3), the delta function is calculated as

$$d(x, y, R) = \sum_{j=1}^{N'_{\text{p}}} |s(\hat{y}_j, \hat{R}_j; x_i)| \delta(y - \hat{y}_j, R - \hat{R}_j)$$
(8)

where N'_{p} indicates the number of the local peak points $(\hat{y}_j, \hat{R}_j; x_i)$. Then, the suppression signal is calculated as

$$s_{\text{sup}}^{\text{TRF}}(x, y; R) = s(x, y, R) - \bar{h}_{\text{rebar}}(y, R) * d(x, y, R)$$
(9)

where $*$ denotes the 2-D convolution operator along y and R. Fig. 4 shows the actual processing flow of rebar extraction and suppression. This scheme enables us to eliminate only the rebar responses and obtain reliable responses caused by the anomalous state, even in a deeper area than the rebar location, which cannot be achieved by the simple window function scheme in (2).

C. Anomaly Detection With Unsupervised Machine Learning

Using the preprocessing scheme for rebar response elimination, we introduced several existing anomaly detection schemes

$$W(R; R_{\text{FL}}, \alpha) = \begin{cases} 1, & (0 \leq R \leq (1-\alpha)R_{\text{FL}}) \\ \frac{1}{2}\left\{1 - \sin\left(\frac{\pi(R - R_{\text{FL}})}{2\alpha R_{\text{FL}}}\right)\right\}, & ((1-\alpha)R_{\text{FL}} < R \leq (1+\alpha)R_{\text{FL}}) \\ 0, & (R > (1+\alpha)R_{\text{FL}}). \end{cases}$$
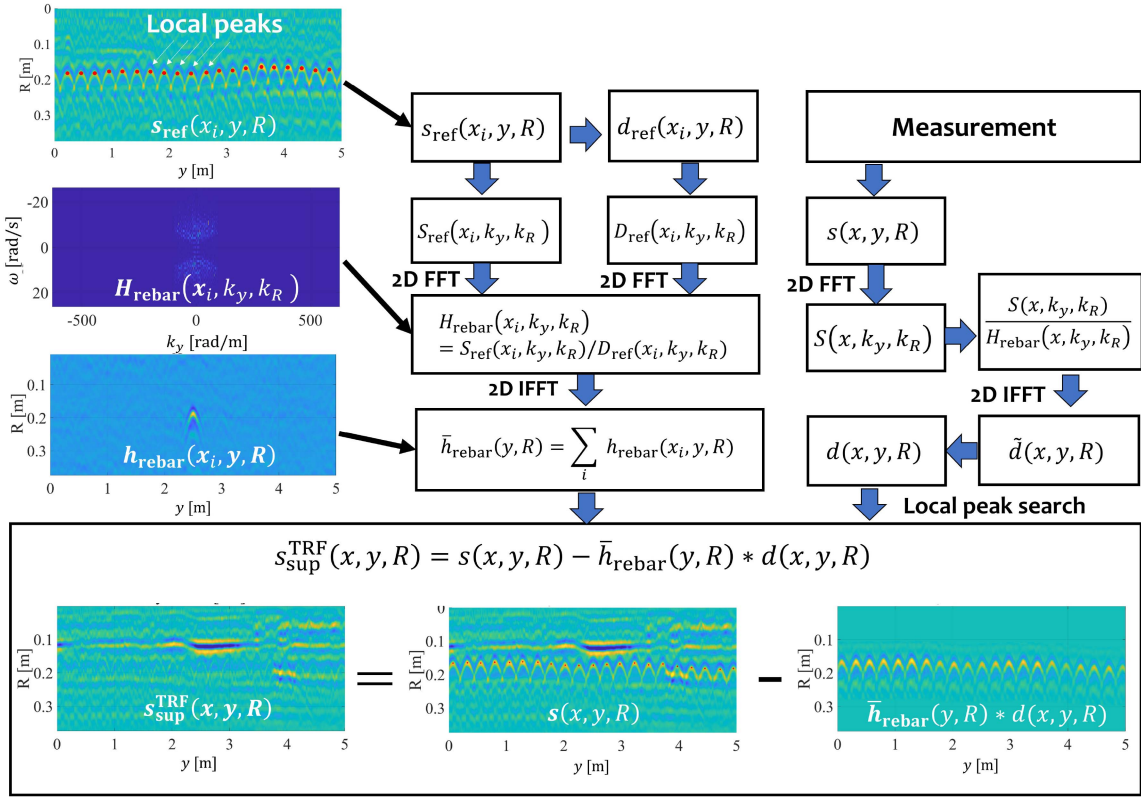(1)

Fig. 4.   Processing flow for rebar response extraction and suppression. The upper left side of the diagram show the generation of referential rebar responses from $s_{\mathrm{ref}}(x_i, y, R)$ via the local peaks profiles as $d_{\mathrm{ref}}(x_i, y, R)$, i.e., corresponding to the process from (3) to (5). The upper right side of the diagram indicates the measurement data processing for extracting local peaks corresponding rebar response, corresponding to the process from (6) to (8). The lower center of the diagram denotes a suppression process of rebar responses, which are generated by referential and measurement data, as in (9).

for microwave GPR data. These are particularly relevant between the asphalt and floorboard, where air cavities, often containing water due to rain penetration, frequently develop from continuous physical pressure. This section details the data processing steps and provides an overview of several existing unsupervised anomaly detection algorithms for addressing such anomalies.

1) Mahalanobis Distance (MD): The MD is known as a promising unsupervised outlier detection method that measures the distance between a sample point and the distribution to consider the covariance matrix of the data [51]. Here, $\boldsymbol{S}(x, y; k_R) \equiv (\Re[S(x, y, k_R)], \Im[S(x, y, k_R)])$ is defined at the specific spatial frequency k_R. Then, the MD $d(x, y)$ is calculated as [51]

$$d(\boldsymbol{S}(x, y; k_R)) =$$
$$\sqrt{(\boldsymbol{S}(x, y; k_R) - \boldsymbol{\mu}(k_R))^T \boldsymbol{\Sigma}^{-1}(k_R)(\boldsymbol{S}(x, y; k_R) - \boldsymbol{\mu}(k_R))} \quad (10)$$

where $\boldsymbol{\mu}(k_R)$ and $\boldsymbol{\Sigma}(k_R)$ denote the mean vector and covariance matrix calculated by all sampled points of $\boldsymbol{S}(x, y; k_R)$, respectively. A sampled area of (x, y) with a large $d(\boldsymbol{S}(x, y; k_R))$ is an outlier, i.e., an abnormal state of the inner structure of the road. Thus, the anomaly index is calculated as

$$\eta^{\mathrm{MD}}(x, y) = d(\boldsymbol{S}(x, y; k_{R,0})) \quad (11)$$

where $k_{R,0}$ denotes the specific spatial frequency, which can be chosen from the center frequency of the transmitted signal.

2) TF Profile-Based Detection: The aforementioned MD approach cannot consider depth-dependent frequency variations, so TF analysis is introduced to validate both the depth and frequency variations of the reflection responses. Simple short-time Fourier transform (STFT) [52] analysis is conducted as

$$S^{\mathrm{TF}}(x, y, R, k_R) = \int_{R-R_{\mathrm{W}}}^{R+R_{\mathrm{W}}} S(x, y, R')e^{-jk_R R'} dR' \quad (12)$$

where R_{W} denotes the coherent processing length along R, which is determined using the pulsewidth of the transmitting signal considering the tradeoff between the depth and frequency resolution. The following 1-D vector is configured to convert the STFT data into input vectors for anomaly detection:

$$\boldsymbol{S}^{\mathrm{TF}}(x, y) =$$
$$[S^{\mathrm{TF}}(x, y, R_1, k_{R,1}), \dots, S^{\mathrm{TF}}(x, y, R_1, k_{R,M_{\mathrm{TF}}})$$
$$S^{\mathrm{TF}}(x, y, R_2, k_{R,1}), \dots, S^{\mathrm{TF}}(x, y, R_2, k_{R,M_{\mathrm{TF}}})$$
$$S^{\mathrm{TF}}(x, y, R_{N_{\mathrm{TF}}}, k_{R,1}), \dots, S^{\mathrm{TF}}(x, y, R_{N_{\mathrm{TF}}}, k_{R,M_{\mathrm{TF}}})] \quad (13)$$

where N_{TF} and M_{TF} denote the total number of samples along R and k_R, respectively, which can be determined by the assumed optical distance range to the existing target and the effective
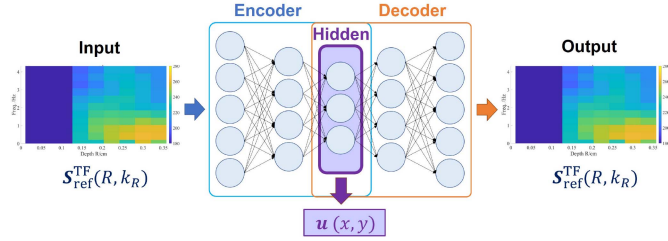
Fig. 5. CAE-based data compression scheme, where the feature vector $\boldsymbol{u}$ of the hidden layer is used for the anomaly detection.

bandwidth of the transmitted pulses. Moreover, to mitigate the influence of surface reflection signals, we can truncate the data by adjusting the starting range to R_1, as depicted in Fig. 5. The cross-correlation coefficient is calculated to assess the similarity to the referential data

$$\eta^{\mathrm{TF}}(x,y) = \Re\left[\frac{\boldsymbol{S}^{\mathrm{TF}}(x,y)(\boldsymbol{S}^{\mathrm{TF}}_{\mathrm{ref}})^*}{||\boldsymbol{S}^{\mathrm{TF}}(x,y)||||\boldsymbol{S}^{\mathrm{TF}}_{\mathrm{ref}}||}\right] \quad (14)$$

where * denotes the Hermitian transpose, and $\boldsymbol{S}^{\mathrm{TF}}_{\mathrm{ref}}$ denotes the reference data, which are extracted from an area presumed to be in a normal state. $\Re[x]$ denotes the real part of x.

3) Convolutional Autoencoder (CAE): The TF profile, denoted as $\boldsymbol{S}^{\mathrm{TF}}(x,y)$ is formed using 2-D images and may include noise components. To address this, our study employs a CAE-based data compression scheme [53], which effectively reduces the dimensions of the input vectors. Fig. 5 shows the CAE-based data compression scheme, with TF images as the input and output models. Each unit in the middle (hidden) layer has a low-dimensional feature, which excludes unnecessary or redundant components of $S^{\mathrm{TF}}(x,y,R,k_R)$, e.g., noise, which contributes to more reliable recognition even when using a limited number of data points. Thus, we used this compressed feature of the CAE, in our proposed scheme: First, some of the reference data $\boldsymbol{S}^{\mathrm{TF}}_{\mathrm{ref}}$, considered to be normal state, are used as the training data, and the vectors of middle (hidden) layer are defined as $\boldsymbol{u}_{\mathrm{ref}}$, after the completion of the training phase. Then, the vectors of the middle (hidden) layer of this trained CAE for the unknown data $\boldsymbol{S}^{\mathrm{TF}}(x,y)$ are also defined as $\boldsymbol{u}(x,y) = (u_1, u_2, \ldots, u_N)$. The CCI of CAE is calculated as

$$\eta^{\mathrm{CAE}}(x,y) = \frac{\boldsymbol{u}(x,y)\boldsymbol{u}^*_{\mathrm{ref}}}{||\boldsymbol{u}(x,y)||||\boldsymbol{u}_{\mathrm{ref}}||}. \quad (15)$$

While the CCI measures proximity between data points, it cannot clearly identify outliers. Notably, this CAE process is used as dimension reduction process for the post unsupervised anomaly detection scheme and does not require any training samples. Therefore, no prior knowledge of whether the input data represent normal or abnormal road conditions is necessary in this method, which is advantageous over other supervised learning schemes.

4) DBSCAN: The literature also highlights the DBSCAN algorithm [54] as an effective outlier detection method that groups data points based on their neighboring states. In this scheme, the sample points are divided into three categories, namely, core

points, reachable points, and outliers. A core point $\boldsymbol{p}$ is defined as a point that has at least N_{D} points within a distance of ϵ, including itself. A reachable point $\boldsymbol{q}$ is not a core point but is reachable within ϵ from core point $\boldsymbol{p}$. A point that is not reachable from any core point is an outlier. Given that the dimension of the TF data, $\boldsymbol{S}^{\mathrm{TF}}(x,y)$, includes redundant aspects, we further utilize the dimension-reduced feature vector, denoted as $\boldsymbol{u}(x,y)$ within the DBSCAN algorithm. The anomaly index with DBSCAN is then calculated as

$$\eta^{\mathrm{DBSCAN}}(x,y) = \mathrm{DBSCAN}\left[\boldsymbol{u}(x,y)\right] \quad (16)$$

where the operator $\mathrm{DBSCAN}[*]$ determines the integer index of the cluster of $\boldsymbol{u}(x,y)$.

5) Integrated Index for Anomaly Decision: Considering the anomaly indexes described in Section III-C1–III-C4, we integrate those indexes into one index as $\eta^{\mathrm{INT}}(x,y)$ for the decision making of the anomaly area. Table I summarizes each index for anomaly detection described in Section III-C. Here, we consider that the value of "maximum strength" as $s_{\max}(x,y)$, defined as

$$s_{\max}(x,y) = \max_R |s(x,y,R)|. \quad (17)$$

This index is also useful for anomaly detection. Thus, the four indexes as $s_{\max}(x,y)$, $\eta^{\mathrm{MD}}(x,y)$, $\eta^{\mathrm{TF}}_{\mathrm{norm}}(x,y)$, and $\eta^{\mathrm{CAE}}_{\mathrm{norm}}(x,y)$ are integrated, because $\eta^{\mathrm{DBSCAN}}_{\mathrm{norm}}(x,y)$ highly correlates with the results of $\eta^{\mathrm{CAE}}_{\mathrm{norm}}(x,y)$. To integrate each index, the following normalization scheme is employed so that each index ranges from 0 to a maximum value greater than 0 ($\eta_{\max} > 0$).

$$s_{\mathrm{norm}}(x,y) = \eta_{\max}\left(1 - \frac{s_{\max}(x,y)}{\max\limits_{x,y} s_{\max}(x,y)}\right) \quad (18)$$

$$\eta^{\mathrm{MD}}_{\mathrm{norm}}(x,y) = \eta_{\max}\left(1 - \frac{\eta^{\mathrm{MD}}(x,y)}{\max\limits_{x,y} \eta^{\mathrm{MD}}(x,y)}\right) \quad (19)$$

$$\eta^{\mathrm{TF}}_{\mathrm{norm}}(x,y) = \frac{\eta_{\max}}{2}\left(1 + \eta^{\mathrm{TF}}(x,y)\right) \quad (20)$$

$$\eta^{\mathrm{CAE}}_{\mathrm{norm}}(x,y) = \eta_{\max}\, \eta^{\mathrm{CAE}}(x,y). \quad (21)$$

Then, the integrated index is calculated as follows:

$$\eta^{\mathrm{INT}}(x,y) = s_{\mathrm{norm}}(x,y) + \eta^{\mathrm{MD}}_{\mathrm{norm}}(x,y) + \eta^{\mathrm{TF}}_{\mathrm{norm}}(x,y) + \eta^{\mathrm{CAE}}_{\mathrm{norm}}(x,y). \quad (22)$$

If $\eta^{\mathrm{INT}}(x,y)$ is lower than those obtained in normal area, it indicates the area of (x,y) as a possible anomaly area.

III. EXPERIMENTAL TESTS

A. Experimental Setting and Preprocessing

We tested the rebar suppression and anomaly detection schemes with data acquired using commercial ultrawideband (UWB) radar module on real bridge roads. Fig. 6 shows the measurement process at an investigation site. The pavement surface is scanned using the radar equipment (StructureScan SIR-EZ XT, GSSI Inc). This UWB radar has a 2.7-GHz center frequency and 2.7-GHz bandwidth. Linear dipole transmitter and receiver antennas (60-mm offset) are installed on the lower

TABLE I
FEATURES FOR EACH ANOMALY DETECTION ALGORITHM

Method (Index)	Input		Output
	Feature	Dimensions	
MD (η^{MD})	Frequency data	N_{F}	Distance (Continuous)
TF (η^{TF})	TF data	$N_{\mathrm{F}} \times N_{\mathrm{T}}$	CCI (Continuous)
CAE (η^{CAE})	TF data with CAE compression	N_{H}	CCI (Continuous)
DBSCAN (η^{DBSCAN})	TF data with CAE compression	N_{H}	Number of cluster (Discrete)
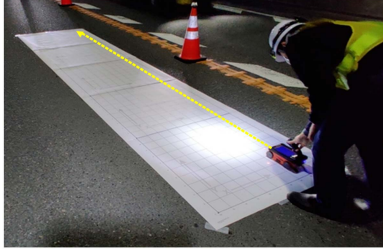
Fig. 6. Measurement scene using the GPR at the pavement on the bridge.

(a)

SCAN 1   SCAN 2   SCAN 3

(b)

Fig. 7. Measurement site in Shimizu bridge area at Kanagawa prefecture. Each scanning region includes an area with surface crack on pavement. (a) Site. (b) Surface crack area.

side of the radar. Two cases were investigated. Case # 1 involves data from the Shimizu River bridge road (Kanagawa Prefecture, November 2021) and Case # 2 is from the Shin-tone River bridge road (Ibaraki Prefecture, October 2022), respectively. In Case # 1, we investigated three different areas, termed as SCAN 1, 2, and 3, and in Case # 2, we measured one specific area termed as SCAN 4. Case # 2 considers prior knowledge about an anomalous area; the underside of the bridge has free lime due to water leakage. Notably, if the conductivity of the asphalt or concrete floorboard is approximately 0.001 S/m, as referred from [6], the penetration depth is calculated as 306.2 mm, and the transmitted signals can sufficiently penetrate the center of the floorboard or rebar position (a depth of approximately 200 mm).

B. Case # 1 : Shimizu Bridge Road

First, we investigate the Case # 1. Reflection data (SCAN 1, SCAN 2, and SCAN 3) are acquired from three different areas (0 m $\leq x \leq$ 2.6 m and 0 m $\leq y \leq$ 5.0 m with 200 and 100 mm spacings along the x- and y-axes, respectively). Then, 700 (14 $\times$ 50) location samples are investigated for anomaly detection. Fig. 7 shows each scan area and the surface crack region within these areas. Water may leak into the asphalt because of cracks on the pavement surface, and then, accumulate at the boundary area between the asphalt and the concrete floorboard, as shown in Fig. 1.

1) Results: Rebar Response Suppression: We assess the preprocessing of B-scan data for rebar response suppression, as described in Section II-B. Fig. 8 shows three examples of the studied B-scan data and the extracted rebar responses, calculated as $h_{\mathrm{rebar}}(x_i, y, R)$ in Section II-B1. As shown in Fig. 8, a single rebar response is extracted from the B-scan data of each scan area and included many overlapping hyperbolic responses of rebar reflections, however, unnecessary responses caused by other reflection effects are also included. Then, Fig. 9 shows the responses averaged using the reference rebar responses in
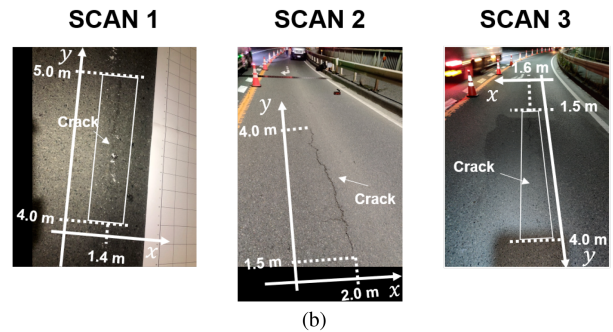
Fig. 8 and demonstrates that the unnecessary responses are considerably suppressed by the coherent averaging effect.

Fig. 10 shows a comparison of the suppression results of the simple roll-off filter approach in (1), and the TRF-based approach in (9) using the averaged rebar responses in Fig. 9. Although the roll-off filter method can suppress the rebar responses over the specific depth, some responses remain around the boundary responses between the asphalt and floorboard. In addition, this approach can eliminate responses in deeper areas, which may include anomalous signals, for example, those of cracks and water leakage. On the contrary, the TRF-based method exhibits more effective suppression; the boundary responses are removed, and deeper signals are retained. In Fig. 10(f), the relatively strong responses around 3.8 mm $\leq x \leq$ 4.1 mm at $R = 0.2$ m, are retained, which is also observed at Fig. 10(d) but is contaminated by the rebar responses. Thus, the proposed suppression approach can retain anomalous responses in areas deeper than the rebar position.

2) Results: Anomaly Detection: The anomaly detection results of each algorithm are presented, where the rebar response suppression in (9) is applied for all B-scan data. Figs. 11–13 show the spatial profiles obtained using each detection approach for SCAN 1, SCAN 2, and SCAN 3, respectively. Table II shows the roughly estimated locations of the existing surface cracks in
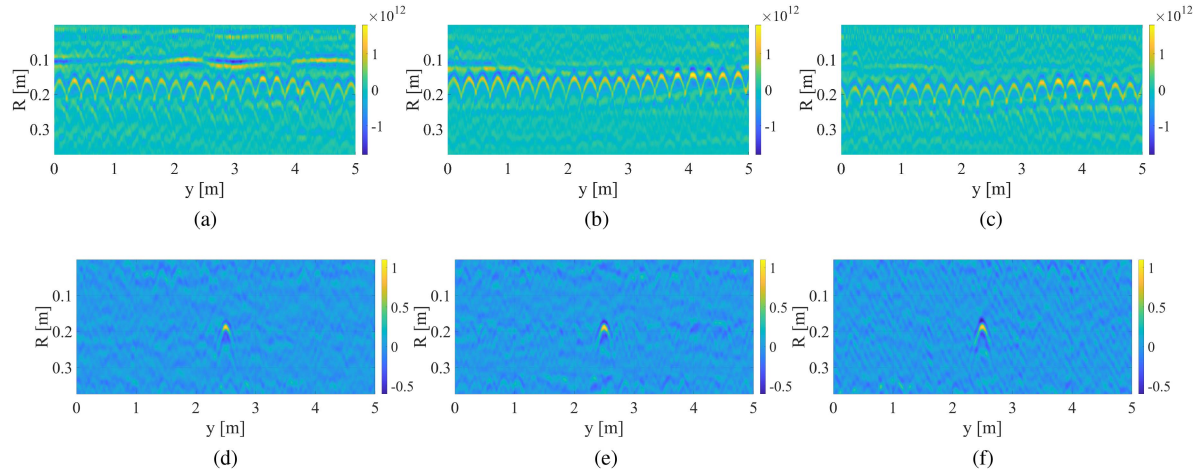
Fig. 8. B-scan data and extracted rebar responses by the proposed scheme. First row: B-scan data. Second row: Extracted rebar responses. (a) SCAN 1, $x = 60$ mm. (b) SCAN 2, $x = 180$ mm. (c) SCAN 3, $x = 60$ mm. (d) SCAN 1, $x = 60$ mm. (e) SCAN 2, $x = 180$ mm. (f) SCAN 3, $x = 60$ mm.
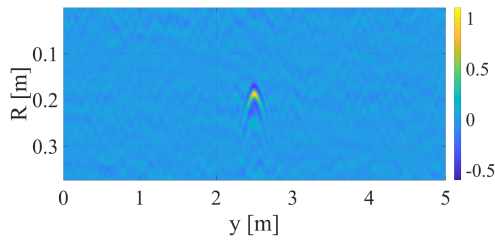

Fig. 9. Averaged rebar responses as $\bar{h}_{\mathrm{rebar}}(y, R)$.

TABLE II
ROUGHLY ESTIMATED AREA CONFIRMED WITH SURFACE CRACK IN EACH SCAN

	$x/$m	$y/$m
SCAN 1	1.4	$4.0 \leq y \leq 5.0$
SCAN 2	2.0	$1.5 \leq y \leq 4.0$
SCAN 3	1.6	$1.5 \leq y \leq 4.0$

TABLE III
PARAMETERS USED IN EACH ANOMALY DETECTION ALGORITHM

Index	Parameter	Value
η^{MD}	$k_{R,0}$	103 rad/m
η^{TF}	R_{W}	30.5 mm
	N_{TF}	42
	M_{TF}	21
η^{CAE}	Number of hidden layers	3
	Number of neurons	(198,100,198)
	Dimension of $\boldsymbol{u}(x, y)$	100
η^{DBSCAN}	N_{D}	60
η^{INT}	$\eta_{\max}$	10

each scan area, which would cause water leakage or air cracks in the asphalt and floorboard, especially in the boundary area between them. Table III also summarizes the parameters used in

each anomaly detection algorithm. In the DBSCAN, $\epsilon = 2.7$ is set.

We first focused on SCAN 1 as shown in Fig. 11. High reflection strengths in the surface crack area in Fig. 11(a) were confirmed, but other areas were also recognized (2.0 m $\leq x \leq$ 2.4 m, 1.5 m $\leq y \leq 2.0$ m). On the contrary, the indexes η^{MD} presented large values along $x = 1.4$ m line, which possibly includes abnormal states caused by water leakage or cracks caused by surface cracking. In addition, η^{TF} and η^{CAE} have a lower correlation index around at $x = 1.4$ m and 2.5 m $\leq y \leq$ 4.0 m, although other areas have a lower correction index. The DBSCAN offers a binary decision that indicates abnormal areas are present not only in the surface crack area, but also in the proximity area around 2.0 m $\leq x \leq 2.4$ m and 1.5 m $\leq y \leq 2.0$ m or 4.0 m $\leq y \leq 5.0$ m. The index η^{INT} is integrated by these indexes, and denotes possible anomalous areas at $x = 1.4$ m and 2.5 m $\leq y \leq 3.0$ m, which is near the area with surface cracking. Second, we discuss the results of the SCAN 2 as seen in Fig. 12. While we could not recognize that the maximum strength [see Fig. 12(a)] and η^{MD} [see Fig. 12(b)] would provide relatively larger values around the surface crack area as $x = 2.0$ m and 1.5 m $\leq y \leq 4.0$ m, η^{TF} and η^{CAE} have a lower correlation index for this area, which was also judged as anomalous area by the DBSCAN, this is because the TF data includes a frequency characteristic with each depth that cannot be assessed by the η^{MD} or maximum strength. For the integrated index η^{INT}, a lower η^{INT} value would be retained around both the surface crack area at $x = 2.0$ m and 1.5 m $\leq y \leq 4.0$ m, and the area at $x = 0.4$ m and 1.0 m $\leq y \leq 2.5$ m, which could have an anomalous state. Finally, as for SCAN 3 (see Fig. 13), several anomaly triggered responses are observed for η^{TF}, η^{CAE}, η^{DBSCAN}, and η^{INT} around the area at $x = 1.6$ m and 1.5 m $\leq y \leq 4.0$ m with surface cracking. Notably, each algorithm has its own advantages and disadvantages; however, the integrated index η^{INT} provides the most reliable results by complementing each advantage and disadvantage. In addition, noticeable reflection responses due to differences in reflectivity between the asphalt and concrete floorboards, as shown in Fig. 10, are common
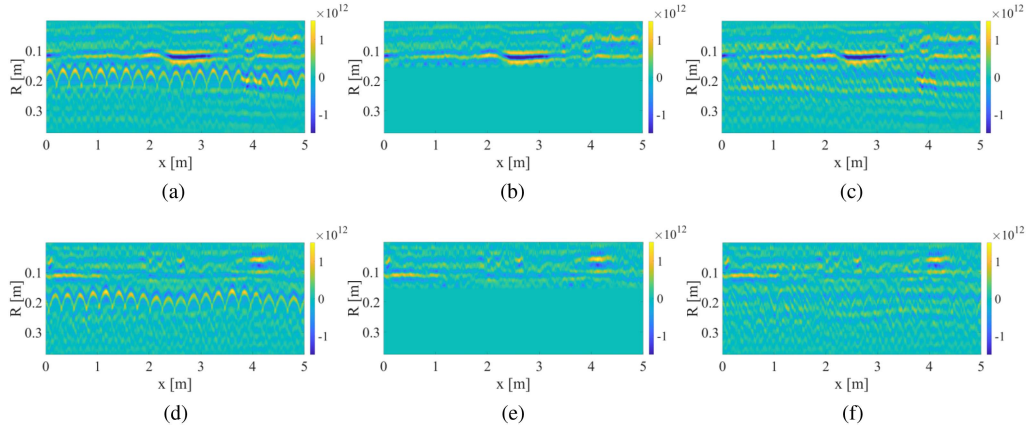
Fig. 10. Suppression examples with each method for B-scan data. First column: Without suppression. Second column: With suppression using (2) as $s_{\text{sup}}^{\text{W}}(x, y, R)$ (Roll-off filter-based). Third column: With suppression using (9) as $s_{\text{sup}}^{\text{TR}}(x, y; R)$ (TF-based). First line: $x = 140$ cm at SCAN 1. Second line: $x = 200$ cm at SCAN 3. (a) Without suppression. (b) With suppression in (2). (c) With suppression in (9). (d) Without suppression. (e) With suppression in (2). (f) With suppression in (9).
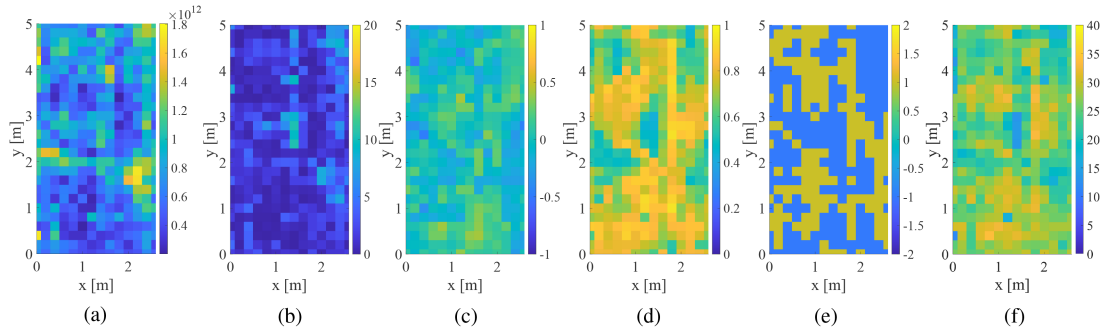

Fig. 11. Anomaly detection results using each algorithm in SCAN 1 at Shimizu bridge (Case # 1). (a) Maximum strength. (b) $\eta^{\text{MD}}(x, y)$. (c) $\eta^{\text{TF}}(x, y)$. (d) $\eta^{\text{CAE}}(x, y)$. (e) $\eta^{\text{DBSCAN}}(x, y)$. (f) $\eta^{\text{INT}}(x, y)$.
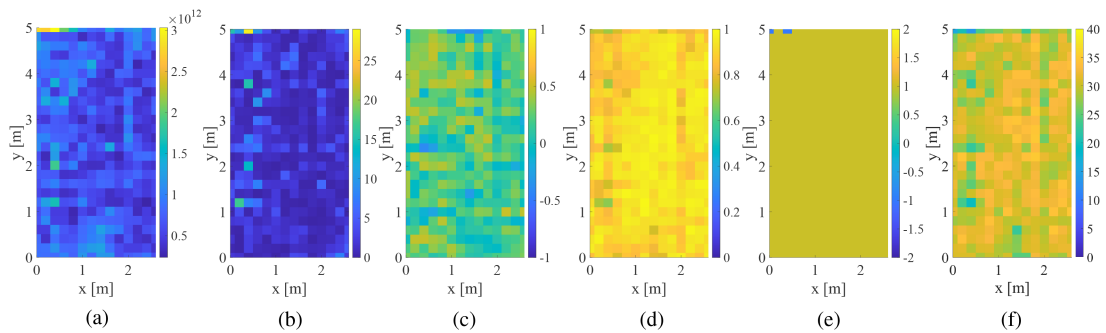

Fig. 12. Anomaly detection results using each algorithm in SCAN 2 at Shimizu bridge (Case # 1). (a) Maximum strength. (b) $\eta^{\text{MD}}(x, y)$. (c) $\eta^{\text{TF}}(x, y)$. (d) $\eta^{\text{CAE}}(x, y)$. (e) $\eta^{\text{DBSCAN}}(x, y)$. (f) $\eta^{\text{INT}}(x, y)$.

elements in healthy and unhealthy pavement states. The responses, shown in Fig. 10, can be eliminated by employing cross-correlation-based comparison methods for normal data, as denoted in η^{TF} or η^{CAE}, or other anomaly detection algorithms. Thus, the correlation-based indexes η^{TF} or η^{CAE} can detect the abnormal response from the normal profile that includes a typical reflection component between asphalt and concrete.

Furthermore, a comparison study for the anomaly detection results from different rebar suppression schemes, namely, the traditional windowing-based scheme, as expressed in (5). Fig. 14 compares the B-Scan data of SCAN 1 at Shimizu Bridge (Case # 1), showing the maximum scattered strength denoted as $s_{\text{max}}(x, y)$ and the integrated anomaly index $\eta^{\text{INT}}(x, y)$, where the B-scan data are extracted from the line of $x = 1.6$
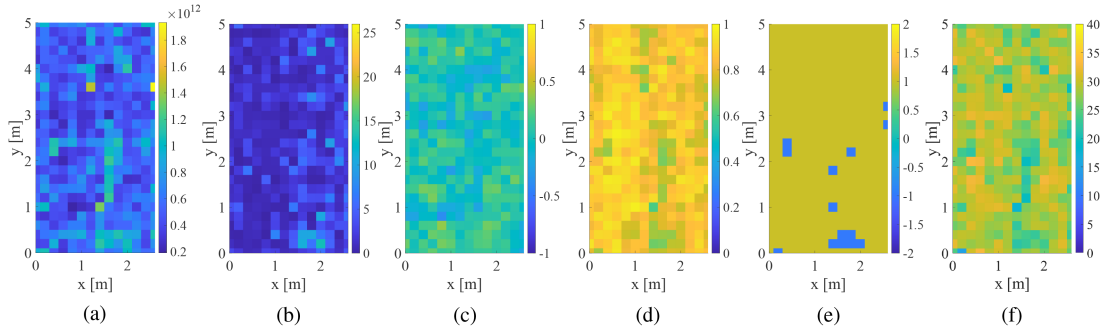
Fig. 13. Anomaly detection results using each algorithm in SCAN 3 at Shimizu bridge (Case # 1). (a) Maximum strength. (b) $\eta^{MD}(x,y)$. (c) $\eta^{TF}(x,y)$. (d) $\eta^{CAE}(x,y)$. (e) $\eta^{DBSCAN}(x,y)$. (f) $\eta^{INT}(x,y)$.
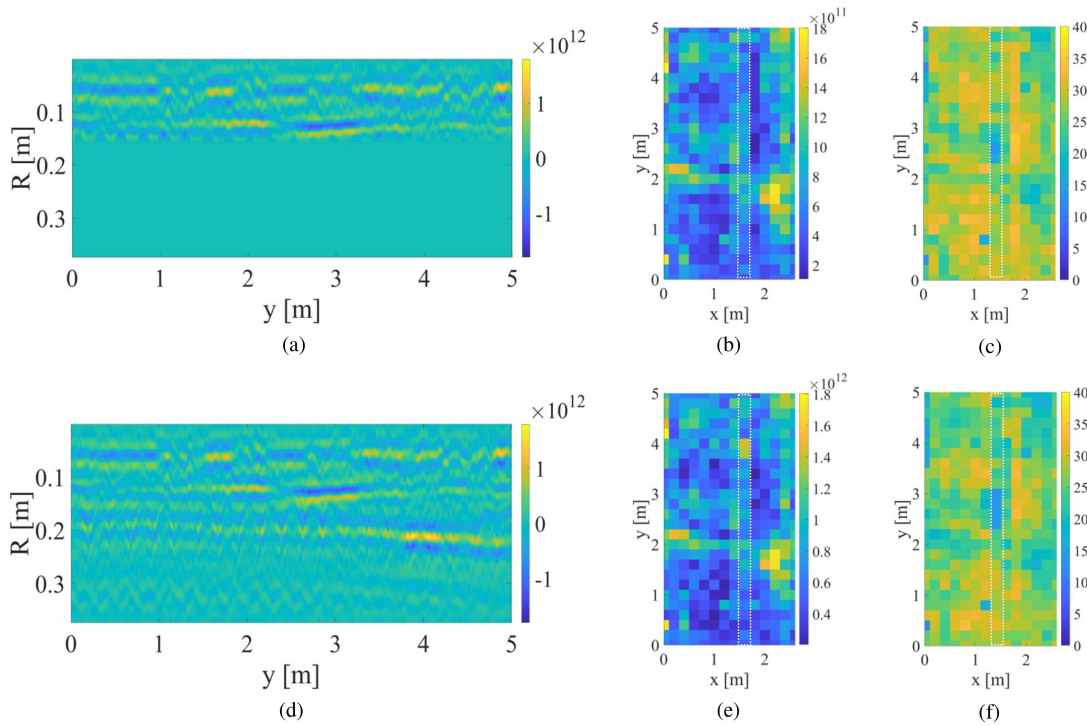

Fig. 14. Comparison for the scattered strength $s_{max}(x,y)$ and the integrated anomaly index as $\eta^{INT}(x,y)$ with each rebar suppression method. White line in (b), (c), (e), and (f) denotes the sampled line of the B-scan in (a) and (d). First line: Rebar suppression with the window-based method in (5). Second line: Rebar suppression with the TRF-based method in (9). (a) B Scan. (b) $s_{max}(x,y)$. (c) $\eta^{INT}(x,y)$. (d) B Scan. (e) $s_{max}(x,y)$. (f) $\eta^{INT}(x,y)$.

m, indicated by white broken line cells. As shown in Fig. 14, the response near 3.8 m $\leq y \leq$ 4.2 m at a depth from 0.22 to 0.26 m, is eliminated by window-based rebar suppression, whereas the TEF-based method retains its response. That response is not analogous to the rebar hyperbolic response, and indicates a possible anomalous area owing to cracks or water leakage, which are also illustrated in the red box in the maximum response $s_{max}(x,y)$. In addition, the anomaly detection for $\eta^{INT}(x,y)$ has higher values in Fig. 14(a), whereas that in Fig. 14(b) has lower values, indicating the anomalous area. Thus, the proposed rebar suppression scheme can detect an anomalous area even at the depth of the rebar position, and it has the potential to detect the anomalous state of the rebar, e.g., corrosion.

C. Case # 2: Shin-Tone Bridge Road

This section describes the detection results for Case # 2 (Shin-tone River bridge site). Fig. 15 shows the measurement and scan areas for SCAN 4 (0 m $\leq x \leq$ 2.0 m and 0 m $\leq y \leq$ 5.0 m with 100 and 100-mm spacing along both the x- and y-axes, respectively). Then, 1050 (21 × 50) location samples are investigated for anomaly detection. The sampled scan area (SCAN 4) includes the free-lime-damaged area at the underside of the bridge, as shown in Fig. 15(b) (0 m $\leq x \leq$ 1.0 m and 1.7 m $\leq y \leq$ 2.0 m). In the upper part of this free-lime-damaged area, i.e., the inner area of the floorboard and asphalt, water leakage will occur owing to surface cracks, and an anomalous state will appear in the floorboard or asphalt layers. The proposed
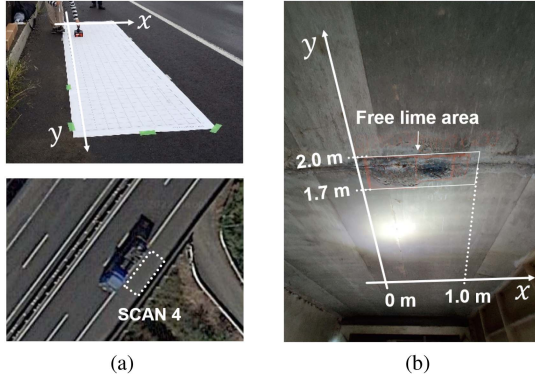
Fig. 15. Measurement site at Shin-Tone Bridge and free-lime area at the bottom side of bridge, which would be caused by water leakage penetrated into the upper concrete floorboard (Case # 2). (a) Site. (b) Free-lime area.

rebar suppression scheme is also applied, and Fig. 16 shows examples of the rebar suppression examples, and this figure demonstrates that they are successfully suppressed, enabling the assessment of reflection responses from the asphalt or floorboard boundary and heterogeneity caused by water leakage or air cracks.

1) Results. Anomaly Detection: Fig. 17 shows each anomaly index profile and the reflection strength profile, where the parameters in each algorithm are shown in Table III, except for the parameter $\epsilon = 1.8$ in the DBSCAN. The rebar response suppression in (9) is applied for all B-scan data. The data samples contain several defections, where the first surface reflection signals could not be sufficiently eliminated, and those data are eliminated from evaluation samples (denoted as white solid cells in 17). As shown in this figure, an area with high index of the maximum strength is identified around the area with the free-lime-damaged region (0 m $\leq x \leq$ 1.0 m and 1.7 m $\leq y \leq$ 2.0 m), which can be also recognized in B-scan data as in Fig. 16. In this area, there should include high contrast materials such as air or water content should be present around the boundary area between the asphalt and floorboard, because it causes water seeping into the inner asphalt area and leads free lime at the bottom of the road in years. Thus, such area should be considered referential anomaly zones, which must be detected by all anomaly detection algorithms.

In addition, all indexes, η^{MD}, η^{TF}, η^{CAE}, and η^{DBSCAN}, also show high anomaly indexes around the free-lime confirmed area. These distinct responses are caused by their significant difference relative to responses in normal areas. It should be noted that the indexes η^{TF} and η^{CAE} show lower correlation indexes, around 1.0 m $\leq x \leq$ 2.0 m and 1.5 m $\leq y \leq$ 2.0 m, which was not identified by the maximum strength or η^{MD}. Since, in the free-lime area, there are linear seams at the bottom along the x-axis, as shown in Fig. 15, there would possibly be a spread anomaly area along the x-axis, inside the asphalt area, which has been demonstrated in the lower area of η^{INT}. In this real-pavement test, we could not determine the presence, location, and nature of defects; however, it is sufficiently reliable that there are some distinct defects, denoted as cracks or water

leakage, inside the asphalt or floorboard because of the distinct free-lime area underside of the road. Then, while it is difficult to evaluate the exact location of the anomaly area or its nature in this case, the obtained anomaly results, commonly judged by several indexes, are reliable to some extent.

In contrast, the indices in other areas (such as $y \geq 2.5$ m), assumed to be in a normal state, maintain relatively high values in η^{INT} compared to the free-lime deterioration area. Despite variations caused by noise or residual effects from incomplete rebar response suppression, as illustrated in Fig. 17(c) or (f) ($y \geq 2.5$ m), their average values ($\eta^{INT} \simeq 35$) are significantly higher than those in the free-lime area ($\eta^{INT} \simeq 15$). Since each index used to generate η^{INT} is derived from the output of each outlier detection algorithm, they exhibit significant differences from the average (normal) data. However, determining the threshold value for these indices, which could be established empirically or through a supervised detection scheme with ground-truth investigation by actually examining the road's interior, remains a crucial point. It would also be beneficial to incorporate a quantitative imaging scheme, such as the inverse scattering scenario mentioned in [32], to characterize the material properties of anomalous objects in areas with lower η^{INT}.

IV. COMPARISONS WITH RELATED WORKS

This section describes a qualitative comparison for other existing related works to show the novelty or contribution of this study. As described in Section I, few studies have focused on anomaly detection using microwave data, whereas vision-based (e.g., optical image) or vibration-based (sound or ultrasound) detection schemes have been investigated [40].

We initially focused on vision-based data, such as using camera images or laser reflections (see Table IV). The vision-based approaches enable quick and large-scale surveying, are useful for determining the size and number of anomalies, and are less expensive than other tools. However, this approach cannot provide the depth and shape of anomalies inside concrete media. Furthermore, the accuracy largely depends on the optical environment, for example, strong back lighting or shadows.

In addition, many studies have used vibration response such as sound or ultrasound techniques, such as a deep neural network [41], [42], image analysis [44], or public database [55] (see Table IV). These approaches can measure a response from an anomalous state buried in concrete media, are more cost-effective than optical or microwave sensors and can achieve real-time detection or feedback. However, contact measurement is needed to avoid noise due to an air gap, and accurate image reconstruction requires prior knowledge of the propagation velocity of background media.

Conversely, few studies have used microwave data-based anomaly detection scheme with a machine learning scheme. A previous study [56] introduced the RFID-based pavement monitoring, which is mounted on the investigation vehicle but this was not oriented to investigate an anomalous state for an inner area in asphalt or floorboard. Microwave-based monitoring tools enable rapid noncontact measurement and large-scale surveying with a deep penetration depth of > 500 mm for low
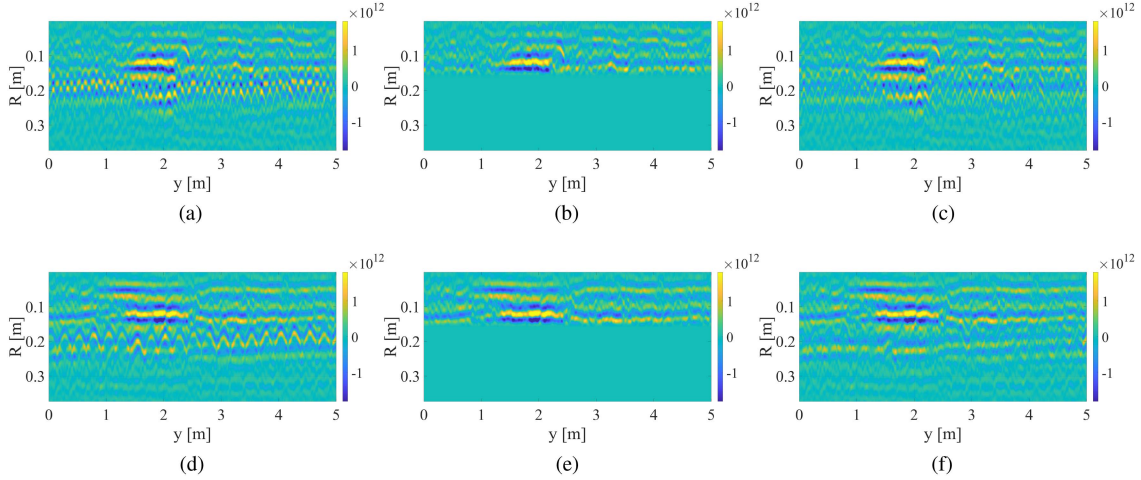
Fig. 16. Suppression examples with each method for B-scan data in Case # 2. First column: Without suppression. Second column: With suppression using (2) as $s_{\text{sup}}^{\text{W}}(x, y, R)$ (Roll-off filter-based). Third column: With suppression using (9) as $s_{\text{sup}}^{\text{TR}}(x, y; R)$ (TRF-based). First line: $x = 0$ cm. Second line: $x = 30$ cm. (a) Without suppression. (b) With suppression in (2). (c) With suppression in (9). (d) Without suppression. (e) With suppression in (2). (f) With suppression in (9).
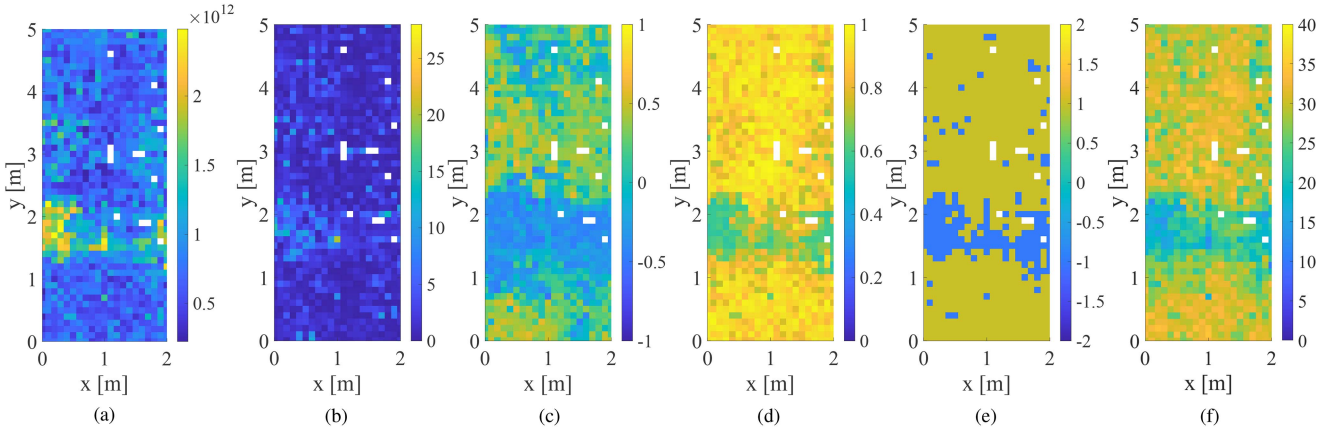

Fig. 17. Anomaly detection results using each algorithm in SCAN 4 at Shin-Tone bridge (Case # 2). White solid cells are defected data samples. (a) Maximum strength. (b) $\eta^{\text{MD}}(x, y)$. (c) $\eta^{\text{TF}}(x, y)$. (d) $\eta^{\text{CAE}}(x, y)$. (e) $\eta^{\text{DBSCAN}}(x, y)$. (f) $\eta^{\text{INT}}(x, y)$.

TABLE IV
QUALITATIVE COMPARISON WITH OTHER RELATED WORKS

Measurement Data	Target	Classifier	References
Vision-based	Surface crack	U-net CNN	[33]
Vision-based	Surface crack	Random forests	[34]
Vision-based	Surface crack	Semantic sedimentation	[35], [37]
Vibration-based (Sound)	Internal anomaly	DNN	[41]
Vibration-based (Ultrasound)	Crack depth	N/A	[43]
Vibration-based (Ultrasound)	Air crack	Image analysis	[44]
Vibration-based (Ultrasound)	Internal defects	DNN	[42]

loss concrete media. This much wider beam compared with that of an optical laser enables the investigation of the inner state of pavement with fewer observation points. However, microwave-based detection has limited spatial resolution compared with that of vision or vibration based image, and has a relatively high cost than other tools. While microwave-based investigations offer clear advantages, existing studies have predominantly focused

on image-based recognition of buried objects, heavily reliant on the selected propagation model, namely, the relative permittivity of the background media or clutter responses from rebar. Furthermore, as outlined in Section I, studies employing supervised machine learning approaches using GPR data [45], [46] have shown that their accuracy largely depends on the selected training dataset, which should encompass various types of anomalies

and road structures. In addition, these schemes often fail to differentiate strong rebar responses from more moderate responses caused by anomalies, complicating the identification of nonrebar anomalies such as air cracks or water voids. Conversely, the method proposed in this article relies on unsupervised anomaly detection, suitable for a variety of road and anomaly structure models, where rebar and anomaly responses are effectively separated using a TRF-based suppression scheme.

V. CONCLUSION

This article introduces an unsupervised anomaly detection scheme by microwave GPR data to detect suspicious areas in a pavement without computationally demanding imaging analysis. First, a TRF-based rebar response extraction and rejection scheme, which is characterized by averaged rebar hyperbolic responses, has been implemented to extract only responses caused by anomalous states, including air cracks and water leakage. Our proposed suppression scheme eliminated high-magnitude clutter (rebar responses) to assess only the responses from the boundary area between the asphalt and floorboard, which usually included air cracks, water leakage, and other abnormal states. Then, several anomaly detection algorithms were applied to the processed B-scan data, including a deep-learning-based feature extraction method using a CAE and a representative nonlinear outlier detection algorithm (DBSCAN).

The experimental evaluation of two real road sites demonstrated that our scheme effectively recognized a possible anomalous state, indicated by the presence of surface cracks and free-lime damage. However, this evaluation finding was hardly justified because we could not confirm the state of the inner area of the pavement. Nonetheless, this study includes significant contribution to the actual pavement GPR investigations for the following reasons.

1) First, since we eliminated the responses from asphalt surfaces and rebar responses, the anomaly indexes reliably denote the differences from the normal state, focusing on the reflectivity or dielectric property change of the boundary area between asphalt and floorboard shown in the measured B-scan data.

2) The common responses between normal and abnormal states in B-scan can be eliminated by introducing the simple cross-correlation coefficient especially for η_{TF} and η_{CAE}. While these indexes are very simple, they are reliable and demonstrate clear evidence of the proof of principle.

3) Finally, we used this scheme to investigate anomalies in the Shin-tone bridge as this includes the observation data for the area with the free-lime phenomena at the bottom of the road. In these areas, high contrast materials such as air or water content around the boundary area should be present between the asphalt and floorboard because of long-term water seepage into the inner asphalt area and formation of free lime at the bottom of the road. These areas must be referential anomaly zones, which have been detected as outliers by all anomaly detection algorithms, that is, the proposed scheme, including all anomaly

indices, would offer clear and convincing evidence for anomaly detection in aging real pavement monitoring.

Notably, with a deeper penetration length using the frequency band assumed in this study (2.7 GHz), an effective noise-reduction filter, e.g., a matched filter or synthetic aperture, can enhance the equivalent SNR, thereby producing a more reliable or accurate radar and inverse scattering reconstruction. It is also noteworthy that our proposed scheme, being unsupervised, can accommodate different road scenarios, such as variations in thickness, relative permittivity, or rebar arrangement, if we could collect sufficient datasets of the normal state of the road. And such an assumption is not impractical since a large portion of investigated road areas are typically in a normal state, barring major collapses or similar events.

REFERENCES

[1] L. Yi, L. Zou, K. Takahashi, and M. Sato, "High-resolution velocity analysis method using the l-1 norm regularized least-squares method for pavement inspection," *IEEE J. Sel. Topics Appl. Earth Observ. Remote Sens.*, vol. 11, no. 3, pp. 1005–1015, Mar. 2018.

[2] A. Valls, F. García, M. Ramírez, and J. Benlloch, "A combined use of GPR data with historical archives for identifying pavement construction periods of Valencian Silos (16th Century, Spain)," *IEEE J. Sel. Topics Appl. Earth Observ. Remote Sens.*, vol. 9, no. 1, pp. 98–107, Jan. 2016.

[3] C. L. Bastard, V. Baltazart, Y. Wang, and J. Saillard, "Thin-pavement thickness estimation using GPR with high-resolution and superresolution methods," *IEEE Trans. Geosci. Remote Sens.*, vol. 45, no. 8, pp. 2511–2519, Aug. 2007.

[4] T. Yamaguchi, T. Mizutani, K. Meguro, and T. Hirano, "Detecting subsurface voids from GPR images by 3-D convolutional neural network using 2-D finite difference time domain method," *IEEE J. Sel. Topics Appl. Earth Observ. Remote Sens.*, vol. 15, pp. 3061–3073, 2022.

[5] A. J. Bahr, "Nondestructive microwave evaluation of ceramics," *IEEE Trans. Microw. Theory Techn.*, vol. 26, no. 9, pp. 676–683, Sep. 1978.

[6] R. Zoughi, *Microwave Nondestructive Testing and Evaluation*. Amsterdam, The Netherlands: Kluwer, 2000.

[7] G. Roqueta, L. Jofre, and M. Q. Feng, "Analysis of the electromagnetic signature of reinforced concrete structures for nondestructive evaluation of corrosion damage," *IEEE Trans. Instrum. Meas.*, vol. 61, no. 4, pp. 1090–1098, Apr. 2012.

[8] B. Gao, H. Zhang, W. L. Woo, G. Y. Tian, L. Bai, and A. Yin, "Smooth nonnegative matrix factorization for defect detection using microwave nondestructive testing and evaluation," *IEEE Trans. Instrum. Meas.*, vol. 63, no. 4, pp. 923–934, Apr. 2014.

[9] N. N. Qaddoumi, W. M. Saleh, and M. Abou-Khousa, "Innovative near-field microwave nondestructive testing of corroded metallic structures utilizing open-ended rectangular waveguide probes," *IEEE Trans. Instrum. Meas.*, vol. 56, no. 5, pp. 1961–1966, Oct. 2007.

[10] C. Liu and R. Zoughi, "Adaptive synthetic aperture radar (SAR) imaging for optimal cross-range resolution and image quality in NDE applications," *IEEE Trans. Instrum. Meas.*, vol. 70, pp. 1–7, Oct. 2021, Art. no. 8005107.

[11] J. Laviada, B. Wu, M. T. Ghasr, and R. Zoughi, "Nondestructive evaluation of microwave-penetrable pipes by synthetic aperture imaging enhanced by full-wave field propagation model," *IEEE Trans. Instrum. Meas.*, vol. 68, no. 4, pp. 1112–1119, Apr. 2019.

[12] M. Dvorsky, M. T. A. Qaseer, and R. Zoughi, "Detection and orientation estimation of short cracks using circularly polarized microwave SAR imaging," *IEEE Trans. Instrum. Meas.*, vol. 69, no. 9, pp. 7252–7263, Sep. 2020.

[13] F. Soldovieri, A. Brancaccio, G. Prisco, G. Leone, and R. Pieri, "A Kirchhoff-based shape reconstruction algorithm for the multimonostatic configuration: The realistic case of buried pipes," *IEEE Trans. Geosci. Remote Sens.*, vol. 46, no. 10, pp. 3031–3038, Oct. 2008.

[14] X. Zhuge, A. G. Yarovoy, T. G. Savelyev, and L. P. Ligthart, "Modified Kirchhoff migration for UWB MIMO array-based radar imaging," *IEEE Trans. Geosci. Remote Sens.*, vol. 48, no. 6, pp. 2692–2703, Jun. 2010.

[15] C. Liu, M. T. A. Qaseer, and R. Zoughi, "Permittivity extraction from synthetic aperture radar (SAR) images of multilayered media," *IEEE Trans. Instrum. Meas.*, vol. 70, pp. 1–11, Sep. 2021, Art. no. 8004611.

[16] M. Benedetti, M. Donelli, A. Martini, M. Pastorino, A. Rosani, and A. Massa, "An innovative microwave-imaging technique for nondestructive evaluation: Applications to civil structures monitoring and biological bodies inspection," *IEEE Trans. Instrum. Meas.*, vol. 55, no. 6, pp. 1878–1884, Dec. 2006.

[17] S. Takahashi, K. Suzuki, T. Hanabusa, and S. Kidera, "Microwave subsurface imaging method by incorporating radar and tomographic approaches," *IEEE Trans. Antennas Propag.*, vol. 70, no. 11, pp. 11009–11023, Nov. 2022.

[18] E. Pettinelli et al., "GPR response from buried pipes: Measurement on field site and tomographic reconstructions," *IEEE Trans. Geosci. Remote Sens.*, vol. 47, no. 8, pp. 2639–2645, Aug. 2009.

[19] F. Soldovieri, J. Hugenschmidt, R. Persico, and G. Leone, "A linear inverse scattering algorithm for realistic GPR applications," *Near Surf. Geophys.*, vol. 5, no. 1, pp. 29–41, Feb. 2007.

[20] G. Leone and F. Soldovieri, "Analysis of the distorted born approximation for subsurface reconstruction: Truncation and uncertainties effects," *IEEE Trans. Geosci. Remote Sens.*, vol. 41, no. 1, pp. 66–74, Jan. 2003.

[21] O. M. Bucci, L. Crocco, T. Isernia, and V. Pascazio, "Subsurface inverse scattering problems: Quantifying, qualifying, and achieving the available information," *IEEE Trans. Geosci. Remote Sens.*, vol. 39, no. 11, pp. 2527–2538, Nov. 2001.

[22] G. Ludeno, G. Gennarelli, S. Lambot, F. Soldovieri, and I. Catapano, "A comparison of linear inverse scattering models for contactless GPR imaging," *IEEE Trans. Geosci. Remote Sens.*, vol. 58, no. 10, pp. 7305–7316, Oct. 2020.

[23] P. M. van den Berg and R. E. Kleinman,, "A contrast source inversion method," *Inverse Problems*, vol. 13, pp. 1607–1620, Jul. 1997.

[24] P. M. van den Berg, A. L. van Broehoven, and A. Abubakar, "Extended contrast source inversion," *Inverse Problems*, vol. 15, pp. 1325–1344, 1999.

[25] P. van den Berg, A. Abubakar, and J. Fokkema, "Multiplicative regularization for contrast profile inversion," *Radio Sci.*, vol. 38, pp. 23.1–23.10, 2003.

[26] S. Sun, B. J. Kooij, and A. G. Yarovoy, "Linearized 3-D electromagnetic contrast source inversion and its applications to half-space configurations," *IEEE Trans. Geosci. Remote Sens.*, vol. 55, no. 6, pp. 3475–3487, Jun. 2017.

[27] R. Marklein, J. Miao, M. Rahman, and K. J. Langenberg, "Inverse scattering and imaging in NDT: Recent applications and advances," in *Proc. 9th Eur. Conf. NDT*, Sep. 2006, pp. 1–8.

[28] L.-P. Song, Q. H. Liu, F. Li, and Z. Q. Zhang, "Reconstruction of three-dimensional objects in layered media: Numerical experiments," *IEEE Trans. Antennas Propag.*, vol. 53, no. 4, pp. 1556–1561, Apr. 2005.

[29] R. Persico, G. Pochanin, V. Ruban, A. Orlenko, I. Catapano, and F. Soldovieri, "Performances of a microwave tomographic algorithm for GPR systems working in differential configuration," *IEEE J. Sel. Topics Appl. Earth Observ. Remote Sens.*, vol. 9, no. 4, pp. 1343–1356, Apr. 2016.

[30] M. Ambrosanio, M. T. Bevacqua, T. Isernia, and V. Pascazio, "Performance analysis of tomographic methods against experimental contactless multistatic ground penetrating radar," *IEEE J. Sel. Topics Appl. Earth Observ. Remote Sens.*, vol. 14, pp. 1171–1183, Jan. 2021.

[31] Y. Yamauchi and S. Kidera, "Complex permittivity imaging by incorporating synthetic aperture radar and inverse scattering method for stratified ground medium," *IEEE J. Sel. Topics Appl. Earth Observ. Remote Sens.*, vol. 17, pp. 766–777, Jan. 2024.

[32] K. Suzuki, S. Nakamura, and S. Kidera, "Complex permittivity retrieval approach with radar enhanced contrast source inversion for microwave nondestructive road evaluation," *IEEE J. Sel. Topics Appl. Earth Observ. Remote Sens.*, vol. 17, pp. 476–488, Jan. 2024.

[33] S. L. H. Lau, E. K. P. Chong, X. Yang, and X. Wang, "Automated pavement crack segmentation using U-Net-Based convolutional neural network," *IEEE Access*, vol. 8, pp. 114892–114899, 2020.

[34] Y. Shi, L. Cui, Z. Qi, F. Meng, and Z. Chen, "Automatic road crack detection using random structured forests," *IEEE Trans. Intell. Transp. Syst.*, vol. 17, no. 12, pp. 3434–3445, Dec. 2016.

[35] S. Shim, J. Kim, G.-C. Cho, and S.-W. Lee, "Multiscale and adversarial learning-based semi-supervised semantic segmentation approach for crack detection in concrete structures," *IEEE Access*, vol. 8, pp. 170939–170950, 2020.

[36] S. Wu, J. Fang, X. Zheng, and X. Li, "Sample and structure-guided network for road crack detection," *IEEE Access*, vol. 7, pp. 130032–130043, 2019.

[37] G. Li, J. Wan, S. He, Q. Liu, and B. Ma, "Semi-supervised semantic segmentation using adversarial learning for pavement crack detection," *IEEE Access*, vol. 8, pp. 51446–51459, 2020.

[38] H. Guan et al., "Iterative tensor voting for pavement crack extraction using mobile laser scanning data," *IEEE Trans. Geosci. Remote Sens.*, vol. 53, no. 3, pp. 1527–1537, Mar. 2015.

[39] M. Cheng, H. Zhang, C. Wang, and J. Li, "Extraction and classification of road markings using mobile laser scanning point clouds," *IEEE J. Sel. Topics Appl. Earth Observ. Remote Sens.*, vol. 10, no. 3, pp. 1182–1196, Mar. 2017.

[40] E. A. Martinez-Ríos, M. R. Bustamante-Bello, and L. A. Arce-Sáenz, "A review of road surface anomaly detection and classification systems based on vibration-based techniques," *Appl. Sci.*, vol. 12, no. 19, 2022, Art. no. 9413.

[41] H. Uematsu, Y. Koizumi, S. Saito, A. Nakagawa, and N. Harada, "Anomaly detection technique in sound to detect faulty equipment," *NTT Tech. Rev.*, vol. 15, no. 4, pp. 28–34, 2014.

[42] Y. Wu, Y. Wang, D. Li, and J. Zhang, "Two-step detection of concrete internal condition using array ultrasound and deep learning," *NDT E. Int.*, vol. 139, 2023, Art. no. 102945.

[43] M. A. Franesqui, J. Yepes, and C. García-González, "Ultrasound data for laboratory calibration of an analytical model to calculate crack depth on asphalt pavements," *Data Brief*, vol. 13, pp. 723–730, 2017.

[44] P. van Horssen et al., "Automated quality control of ultrasound based on in-air reverberation patterns," *Ultrasound*, vol. 25, no. 4, pp 229–238, 2017.

[45] N. Q. Hoang, S. Kang, H.-K. Yoon, and J.-S. Lee, "Enhancing anomaly detection in ground-penetrating radar images through reconstruction loss and high-variability," *Results Eng.*, vol. 21, 2024, Art. no. 101874.

[46] J. Yang, K. Ruan, J. Gao, S. Yang, and L. Zhang, "Pavement distress detection using three-dimension ground penetrating radar and deep learning," *Appl. Sci.*, vol. 12, no. 11, 2022, Art. no. 5738.

[47] X. Wei and Y. Zhang, "Autofocusing techniques for GPR data from RC bridge decks," *IEEE J. Sel. Topics Appl. Earth Observ. Remote Sens.*, vol. 7, no. 12, pp. 4860–4868, Dec. 2014.

[48] X. Wei and Y. Zhang, "Interference removal for autofocusing of GPR data from RC bridge decks," *IEEE J. Sel. Topics Appl. Earth Observ. Remote Sens.*, vol. 8, no. 3, pp. 1145–1151, Mar. 2015.

[49] J. Xiao and L. Liu, "Suppression of clutters caused by periodic scatterers in GPR profiles with multibandpass filtering for NDT & E. Imaging enhancement," *IEEE J. Sel. Topics Appl. Earth Observ. Remote Sens.*, vol. 10, no. 10, pp. 4273–4279, Oct. 2017.

[50] J. W. Helton and O. Merino, "Classical control using H^∞ methods: An introduction to design," in *Society for Industrial and Applied Mathematics*. Philadelphia, PA, USA: SIAM, 1998, pp. 23–25.

[51] P. M. Chandra, "On the generalised distance in statistics," *Proc. Nat. Inst. Sci. India*, vol. 2, no. 1, pp. 49–55, 1936.

[52] J. B. Allen, "Short time spectral analysis, synthesis, and modification by discrete Fourier transform," *IEEE Trans. Acoustics, Speech, Signal Process.*, vol. 25, no. 3, pp. 235–238, Jun. 1977.

[53] R. Manassés, L. A. Eugênio, and L. H. Silvério, "A study of deep convolutional auto-encoders for anomaly detection in videos," *Pattern Recognit. Lett.*, vol. 105, pp. 13–22, 2018.

[54] E. Simoudis, J. Han, Fayyad, and M. Usama, "A density-based algorithm for discovering clusters in large spatial databases with noise," in *Proc. 2nd Int. Conf. Knowl. Discov. Data Mining*, 1996, pp. 226–231.

[55] P. Foggia, N. Petkov, A. Saggese, N. Strisciuglio, and M. Vento, "Audio surveillance of roads: A system for detecting anomalous sounds," *IEEE Trans. Intell. Transp. Syst.*, vol. 17, no. 1, pp. 279–288, Jan. 2016.

[56] K. S. Bialkowski and A. M. Abbosh, "Propagation modelling of RFID systems for road monitoring applications," in *Proc. Int. Symp. Antennas Propag.*, Hobart, Australia, 2015, pp. 1–3.

Natsuki Akiyama received the B.E. degree in electronics and information engineering from the University of Electro-Communications, Tokyo, Japan, in 2022. She joined Kikusui Electronics, in 2023.

Takahide Morooka received the B.E. degree in communication engineering and informatics from the University of Electro-Communications, Tokyo, Japan, in 2020, and the M.E. degree in communication engineering and informatics from the Graduate School of Informatics and Engineering, University of Electro-Communications, in 2022.

His research interests include deep learning approaches for detecting anomalies in road infrastructure.

Katsuyoshi Suzuki received the B.E. degree in communication engineering and informatics from the University of Electro-Communications, Tokyo, Japan, in 2022, and the M.E. degree in communication engineering and informatics from the Graduate School of Informatics and Engineering, University of Electro-Communications, in 2024.

His research interest includes inverse scattering and radar signal processing for microwave subsurface applications.

Shouhei Kidera (Senior Member, IEEE) received the B.E. degree in electrical and electronic engineering and the M.I. and Ph.D. degrees in informatics from Kyoto University, Kyoto, Japan, in 2003, 2005, and 2007, respectively.

In 2009, he joined as an Assistant Professor the University of Electro-Communications, Tokyo, Japan, where he is currently a full Professor with the Graduate School of Informatics and Engineering. He was with the Cross-Disciplinary Electromagnetics Laboratory, University of Wisconsin Madison, as a Visiting Researcher in 2016. He was a Principal Investigator of the PRESTO Program of Japan Science and Technology Agency (JST) from 2017 to 2021. His current research interests include advanced radar signal processing or electromagnetic inverse scattering issue for ultrawideband (UWB) 3-D sensor or biomedical applications.

Dr. Kidera was the recipient of the 2012 Ando Incentive Prize for the Study of Electronics, 2013 Young Scientist's Prize by the Japanese Minister of Education, Culture, Sports, Science and Technology (MEXT), and 2014 Funai Achievement Award, 2022 KDDI Foundation Award, Contribution Award, and 2023 RIEC Award. He is a Senior Member of the Institute of Electronics, Information, and Communication Engineers of Japan (IEICE), and the International Union of Radio Science (Union Radio-Scientifique Internationale, URSI), and a Member of the Institute of Electrical Engineering of Japan (IEEJ) and the Japan Society of Applied Physics (JSAP).